Cu(I)/Cu(II) Creutz-Taube Mixed-Valence 2D Coordination Polymers

Ning Li,[‡] Gang Wu,[‡] Shibo Xi,[‡] Fengxia Wei, Ming Lin, Jinjun Qiu, Jin-Cheng Zheng, Jiabao Yi, Debbie Hwee Leng Seng, Coryl Jing Jun Lee, D. V. Maheswar Repaka, Xiaoming Liu, Zicong Marvin Wong, Qiang Zhu, Shuo-Wang Yang and He-Kuan Luo**

N. Li, S. Xi, H.-K. Luo
Institute of Sustainability for Chemicals, Energy and Environment, Agency for Science, Technology and Research, 1 Pesek Road, Jurong Island, Singapore 627833
E-mail: luoh@isce2.a-star.edu.sg

N. Li
Institute of Bioengineering and Bioimaging, Agency for Science, Technology and Research, 31 Biopolis Way, Singapore 138669

G. Wu, Z. M. Wong, S.-W. Yang
Institute of High Performance Computing, Agency for Science, Technology and Research, 1 Fusionopolis Way, 16-16, Singapore 138632
E-mail: yangsw@ihpc.a-star.edu.sg

F. Wei, M. Lin, J. Qiu, D. H. L. Seng, C. J. J. Lee, D. V. M. Repaka, Q. Zhu, H.-K. Luo
Institute of Materials Research and Engineering, Agency for Science, Technology and Research, 2 Fuisionopolis Way, Innovis 08-03, Singapore 138634

J.-C. Zheng
Department of Physics and Fujian Provincial Key Laboratory of Theoretical and Computational Chemistry, Xiamen University, Xiamen, China; Department of Physics and Department of New Energy Science and Engineering, Xiamen University Malaysia, Sepang, Selangor, Malaysia

J. Yi
Global Innovative Centre for Advanced Nanomaterials, School of Engineering, The University of Newcastle, Callaghan, NSW 2308, Australia

X. Liu
Colleague of Chemistry, Jilin University, 2699 Qianjin Street, Changchun, China, 130012

‡ These authors contribute equally to the work.

Keywords: mixed-valent compounds, coordination polymer, metal-organic frameworks, Creutz-Taube, two-dimensional

Abstract:
Graphene-like two-dimensional (2D) coordination polymers (GCPs) have been of central research interest in recent decades with significant impact in many fields. According to classical coordination chemistry, Cu(II) can adopt the dsp^2 hybridization to form square planar coordination geometry, but not Cu(I); this is why so far, there has been few 2D layered structures synthesized from Cu(I) precursors. Herein we report a pair of isostructural GCPs synthesized by the coordination of benzenehexathiol (BHT) ligands with Cu(I) and Cu(II) ions, respectively. Various spectroscopic characterizations indicate that Cu(I) and Cu(II) coexist with a near 1:1 ratio in both GCPs but remain indistinguishable with a fractional oxidation state of +1.5 on average, making these two GCPs a unique pair of Creutz-Taube mixed-valence 2D structures. Based on DFT calculations, we further uncovered an intramolecular *pseudo*-redox mechanism whereby the radicals on BHT ligands can oxidize Cu(I) or reduce Cu(II) ions upon coordination, thus producing isostructures yet with distinct electron configurations. For the first time, we demonstrate that using Cu(I) or Cu(II), one can achieve 2D isostructures, indicating an unusual fact that a neutral periodic structure can host a different number of total electrons as ground states, which may open a new chapter for 2D materials.

1. Introduction

Graphene-like two-dimensional (2D) coordination polymers (GCPs) have been attracting immense attention since their emergence in 2012,[1] and demonstrated promising applications for catalysis, energy storage, sensors, magnetic, and electronic devices.[2] The metal ions in these GCPs adopt square-planar dsp^2 hybridization and tetra-coordination to multidentate aromatic ligands, facilitating d-π conjugation and long-range electron delocalization across the 2D structures.[3]

Ni(II), Cu(II), Co(II), and Pt(II) are the most common metal cations for GCP construction, forming porous 2D Kagomé lattice with various ligands (Figure S1).[4] A different GCP

structure, Cu(II)-benzenehexathiol (BHT, $C_6S_6H_6$), was reported by Huang *et al.*,[4d, 5] which features nonporous 2D layers. The absence of counter ions indicates this Cu(II)-BHT structure to be charge neutral. In other words, each five-membered ring formed by ligand-metal chelation displays a formal charge of -1 and contains a radical.[6] Such Cu(II)-BHT exhibits excellent electrical conductivity up to 1580 S/cm at room temperature, and noteworthy superconductivity at 0.25 K.[5b, 7] Its stoichiometric formula is determined to be $[Cu_3C_6S_6]_n$, with each sulfur coordinating to two Cu ions (see GCP **2** in Figure 1). However, the detailed electronic configurations of these GCPs, such as the actual oxidation state of metal ions and bonding order of ligands, are still topics of extensive debate, which boils down to the fundamental principles of coordination chemistry.[6a]

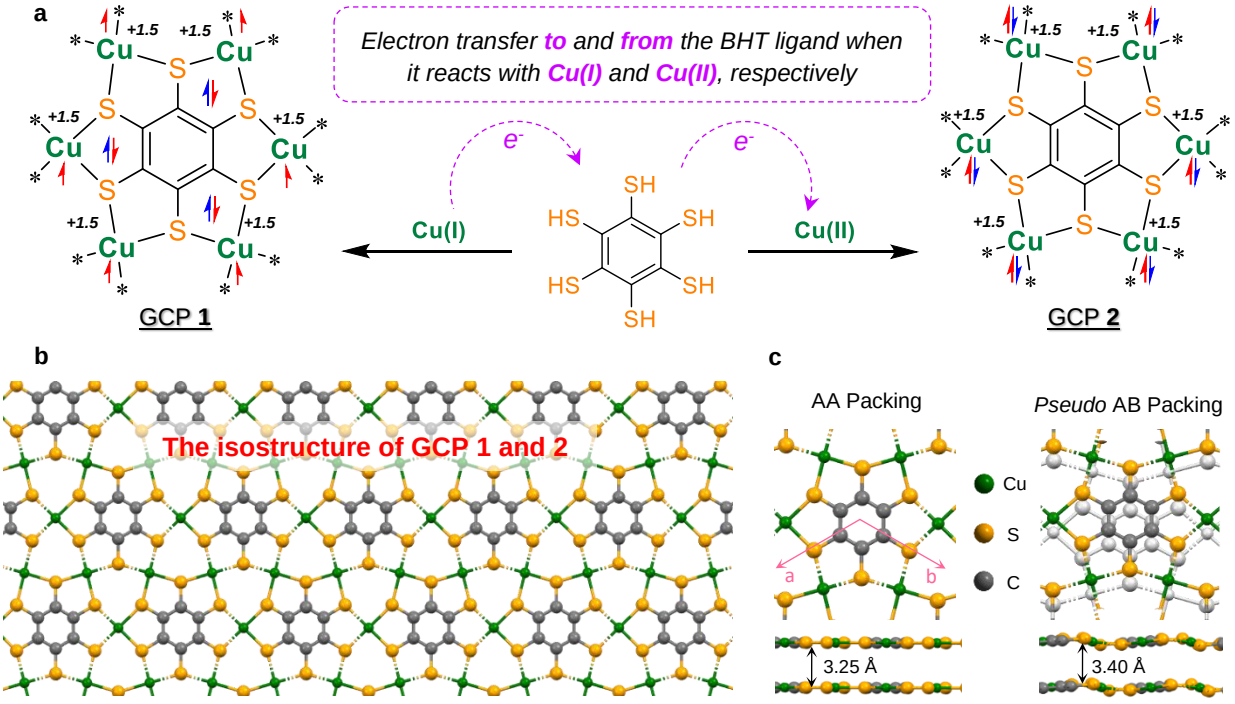

Figure 1. General illustration of synthesis, electron configurations, and crystal structures of Cu-BHT GCPs **1** and **2**: (a) simplified synthetic schemes and proposed electron configurations of GCPs **1** and **2**, with electron transfers between BHT and Cu ions indicated by the arrows in purple; (b) ball-stick representation of a single layer of the isostructural 2D GCPs; (c) the coexisting AA and *pseudo* AB packing patterns in GCP **1** uncovered by DFT calculations.

In comparison to the square-planar d^9 Cu(II), the closed-shell d^{10} Cu(I) displays more complicated coordination geometries, including four-coordinate tetrahedral (sp^3 hybridization), three-coordinate trigonal planar (sp^2), two-coordinate linear (sp), and many others. However, near square-planar coordination of Cu(I) has also been achieved in some sterically hindered

complexes.[8] In view of this, we wonder whether Cu(I) ions could be constrained within a 2D atomic layer to form planar coordinated GCPs. If yes, then how can one synthesize such planar structures and what will be the Cu(I) electron configuration? It seems to be a grand, yet crucial challenge for understanding the nature of 2D coordination chemistry. Very recently, Zhu and co-workers used $[Cu(CH_3CN)_4][BF_4]$ and BHT ligand to construct Cu(I)-BHT coordination, but obtained two semiconducting three-dimensional (3D) structures of chemical formula $[Cu_4C_6S_6]_n$ and $[Cu_{5.5}C_6S_6]_n$, both with interlayer Cu-Cu and Cu-S connectivity.[9]

Herein we report a novel strategy to synthesize Cu(I)-BHT 2D GCP using *in situ* generated $[CuI_2]^-$ anions (**Figure 1**a). The newly formed Cu(I)-BHT structure (GCP **1**) displays a densely packed honeycomb lattice, representing the first example of Cu(I)-derived 2D conjugated coordination polymers. Surprisingly, GCP **1** is isostructural to the aforementioned Cu(II)-BHT counterpart (GCP **2**, Figure 1b).[4d, 5a] To facilitate detailed comparisons, we prepared GCP **2** in our lab using $CuCl_2$ [Cu(II) precursor] and BHT, according to the literature protocol.[5a] We proved that GCPs **1** and **2** are isostructures based on various spectroscopic characterizations. Furthermore, we uncover an intramolecular *pseudo*-redox mechanism during the formation of GCPs **1** and **2**, wherein BHT ligands play the role of oxidants and reductants when they react with Cu(I) and Cu(II) ions, respectively. The as-formed 2D GCPs are typical Creutz–Taube mixed-valence complex structures,[10] with Cu ions interacting with each other via the conjugated BHT ligands in a double-exchange mechanism, averaging to a fractional oxidation state of +1.5 in both cases (Figure 1a). This work addressed a long-standing controversy about metal ion oxidation states in 2D structures, and more importantly unveiled a seemingly peculiar and unrealistic fact that neutral 2D coordination polymers can host a different number of total electrons as ground states without significant structural changes.

2. Results and Discussion

In the synthesis of GCP **1**, copper(I) iodide was employed as the Cu(I) precursor, and excess iodide anions (I^-, from KI) were used to transform the otherwise insoluble CuI into soluble $[CuI_2]^-$ anions in ethanol and water mixture solution, before reacting with BHT under N_2 protection. The presence of large excess of I^- also ensures GCP **1** was synthesized solely from Cu(I)-precursor and BHT, because I^- is a strong antioxidant and able to prevent Cu^+ from being oxidized to Cu^{2+} in solution. Interestingly, the powder X-ray diffraction profile of GCP **1** is identical to the reported Cu(II)-BHT counterpart (GCP **2**), indicating their similar honeycomb-like 2D atomic structures. Field emission scanning electron microscope (FESEM) imaging shows the morphology of GCP **1** crystallites to be hollow hexagonal nanotubes, with

a few hundred nanometers cross-section diameter, microns in length, and 50 – 100 nm tube wall thicknesses (**Figure 2**a and b). Transmission electron microscope (TEM) further confirms such nanotube morphology, where most rod-like particles display hollowness with openings on both ends (Figure 2c). Meanwhile, the in-house synthesized GCP **2** shows solid micro-rods morphology, similar to reported observations (Figure S2).[5a] The interlayer distance of GCP **1** was determined to be *ca.* 3.4 Å by high-resolution TEM (Figure 2d), also comparable to that of GCP **2** in the literature.[5b] No potassium or iodine were detected by energy-dispersive X-ray spectroscopy (FESEM-EDX), indicating absence of counter ions. Elemental mapping shows compositional homogeneity of Cu, S, and C throughout the polycrystalline samples (Figure S3). The Cu:S atomic ratio in GCP **1** was quantified as 0.48:1, agreeing well with that of GCP **2** (i.e. 0.5:1). Combined with the 16.5 wt.% carbon content determined by elemental analysis, these results clearly suggest the $[Cu_3C_6S_6]_n$ chemical formula for both GCPs.

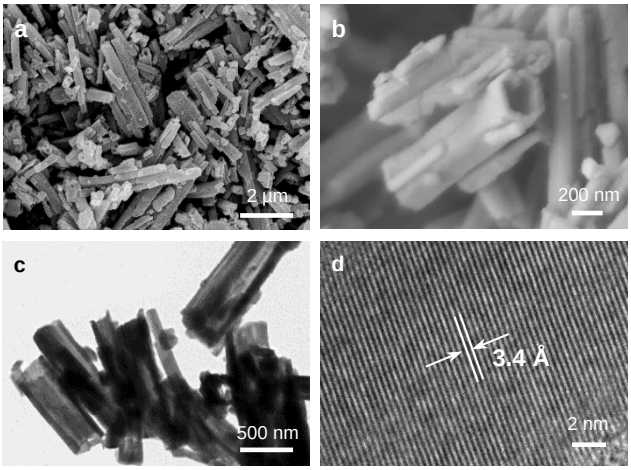

Figure 2. Morphology of GPC **1**: (a and b) FESEM images with different magnifications; (c) TEM image confirming the hollow tubular morphology, and (d) high-resolution TEM image with inter-layer spacing of 3.4 Å indicated.

Powder X-ray diffraction (pXRD) of GCP **1** shows well-defined sharp peaks in the 10 – 40° range (**Figure 3**a). Compared to GCP **2** with a similar diffraction pattern, the isostructural GCP **1** exhibits higher crystallinity,[5a] likely due to the *in situ* formed linear $[CuI_2]^-$ anions that drastically slow down the coordination reaction with BHT ligands. Similar crystallinity enhancement was also observed by Park *et al.*,[11] wherein they used ethylenediamine to slow down the coordination reaction between Cu(II) and hexahydroxybenzene ligands. Our pXRD fitting confirms that the 2D layers in both GCPs adopt a honeycomb structure with the near square-planar Cu ions coordinated to four S atoms and each BHT unit surrounded by six Cu

(Figure 1b). In addition, two different interlayer stacking patterns were identified by pXRD fittings. In one case, neighboring 2D layers align perfectly along the *c*-axis with a 3.25 Å interlayer distance determined by DFT calculation (AA stacking, Figure 1c). In the other case, there is a slight displacement between adjacent layers (*pseudo* AB stacking, Figure 1c), and the interlayer distance enlarges to 3.40 Å. The latter constitutes the majority in the sample (71.9% estimated by XRD peak integration), due to its slightly lower energy level than the former by 2.1 kJ/mol per $[Cu_3C_6S_6]$ unit cell determined by HSE06 functional. The pXRD fitting results agree with the TEM characterization, with most interlayer distances measuring *ca.* 3.4 Å. The 2D layers in *pseudo* AB stacking are not perfectly coplanar based on the high accuracy DFT calculation. Instead, two out of the six Cu ions in the $[Cu_6C_6S_6]$ unit reside slightly above the BHT plane, whereas their *para*-positioned Cu ions reside below, displaying a *chair*-like conformation. It is worth noting that pXRD fitting sometimes is not sensitive enough for atomistic structure resolution, and further verification with precise theoretical modelling and simulation is essential.

X-ray photoelectron spectroscopy (XPS) was also employed to identify the elements and their chemical states on surface. The survey scan revealed Cu, S, and C elements (Figure S4) in both GCPs, although trace O was also detected, possibly from oxygen or water molecules adsorbed on the surface (Figure S5). A high-resolution scan of the Cu *2p* region shows well-resolved peaks at 933.1 and 953.1 eV for GCP **1** (Figure 3b), resembling that of GCP **2** (Figure S6b),[4d] indicating identical Cu states in these two structures prepared from Cu(I) and Cu(II) precursors respectively. Deconvolution of the Cu *2p* signals further reveals two additional broad peaks at around 935.0 and 955.0 eV (Figure 3b and S6b, in orange color), suggesting the coexistence of Cu(I) and Cu(II) in both GCPs. This finding differs from the assumption in the previous work, wherein the authors speculated the Cu(II) ions to be reduced to Cu(I) in GCP 2,[4d] also disagreeing with their later report where Cu(II) magnetic susceptibility was measured and calculated.[5b] In addition, the satellite signals produced by Cu(II) species were also detectable in the spectra (Figure 3b and S6b, in pink color), which further confirms the coexistence of Cu(I) and Cu(II). The ratio of Cu(I):Cu(II) is estimated to be about 1:1 by XPS peak integration. Given the strict N_2 protection and presence of large excess of iodide anions, oxidation of Cu(I) is not possible during the synthesis. Therefore, we attribute the presence of Cu(II) features in GCP **1** to the Cu(I)-to-BHT electron transfer upon coordination, which can be described as an intramolecular *pseudo*-oxidation, causing some apparent oxidation of Cu(I) ions to display Cu(II) characters.[6a]

X-ray absorption near edge structure (XANES) and extended X-ray absorption fine structure (EXAFS) were employed to further unveil the Cu coordination environment in GCPs **1** and **2** in bulk. The rather flattened white line in the Cu K-edge XANES spectra (Figure 3c and S7b, in green color) suggests extensive electron delocalization across the 2D layers in both GCPs, in sharp contrast to the well-defined resonance peaks of the insulating Cu_xO (x = 1 or 2) references and other Cu-MOFs in the literature.[12] Meanwhile, we noted a shift of +0.5 for the Cu oxidation state to +1.5 on average compared to the Cu_2O reference for GCP **1**, estimated based on the Cu XANES K-edges (inset to Figure 3c), which further indicates the coexistence of Cu(I) and Cu(II) with ~1:1 ratio.[13] A similar K-edge position (i.e., between the Cu_2O and CuO references) was also seen for GCP **2** (Figure S7b). Such an observation echoes the XPS-derived claim that both Cu(I) and Cu(II) characters exist in GCPs **1** and **2**. In their corresponding Fourier-transform EXAFS spectra, both GCPs exhibit a prominent peak at 1.87 Å arising from the tetra-coordinated Cu-S bonds, and several other minor peaks assigned to higher-shell Cu-C and Cu-Cu scatterings (Figure S8). Our data fitting suggests an average Cu coordination number of 4.2(5) and Cu-S bond length of 2.287(9) Å in GCP **1**, and 4.0(5) and 2.292(8) Å for GCP **2**, both in accordance with the near square-planar coordination geometry.

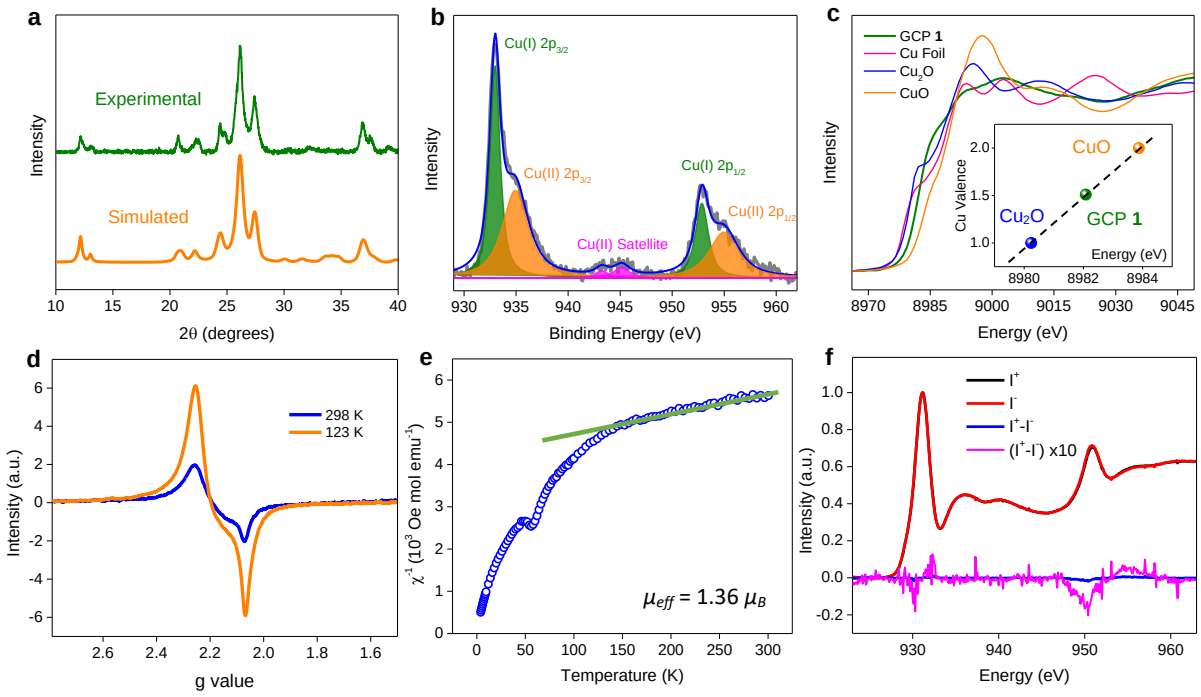

Figure 3. Spectroscopic characterizations of GCP **1**: (a) powder XRD patterns obtained from experiment and simulation; (b) high-resolution XPS scan of the Cu *2p* region and deconvoluted signals; (c) Cu K-edge XANES spectra with inset indicating the average Cu oxidation state determined using the Cu K-edge energy shift; (d) ESR spectra measured at different temperatures; (e) magnetic susceptibility with μ_{eff} calculated as $1.36\mu_B$ for each Cu center based

on Curie-Weiss Law; (f) X-ray magnetic circular dichroism (XMCD) spectra. Comparisons between GCP **1** and **2** on these spectroscopic characterizations were given in Figures S6-S11 in the Supporting Information.

Electron spin resonance (ESR) was further employed to probe the presence of unpaired electrons in these two GCPs. As shown in Figure 3d and S9b, only the Cu(II) 3*d* electron signals at g = 2.2 were observed. The signal intensity increases along with decreasing temperature, implying no long-range magnetic ordering within the experimental temperature range (123 – 298 K).[14] The absence of ESR signal at g = 2.0 indicates no radicals exist in the five-membered coordination rings. In other words, the radicals commonly found on BHT ligands have either relocated away or paired up in these two GCPs. Furthermore, we measured their magnetic susceptibilities to gain insight into the unpaired electrons on metal ions and their couplings. The magnetic behaviors of these two GCPs appear similar (Figure 3e and S10b). Both exhibit paramagnetism above 150 K and large negative Curie temperatures, suggesting antiferromagnetic (AFM) coupling of the Cu ions.[15] This conclusion is also supported by the X-ray magnetic circular dichroism (XMCD) spectra (Figure 3f and S11b), and agrees with our DFT calculations, i.e., the intralayer Cu ions are ferromagnetically (FM) coupled but interlayer AFM as ground states. At the same time, the liquid oxygen spoor was detected around 52 K, suggesting that oxygen had not been entirely eliminated from the samples.[16] Besides, the fitted magnetic susceptibilities (μ_{eff}) for each Cu center in GCP **1** and **2** are 1.36 and 0.51 μ_B respectively, indicating the different electron configurations of these two isostructures. As expected, such μ_{eff} values are also smaller than that of free Cu^{2+} ions (2.73 μ_B), because of the presence of Cu^{+} feature and strong electron coupling in highly conjugated compounds like GCPs **1** and **2**.

In conjugated coordination polymers, defining a redox process is metal-centered or ligand-centered is challenging. Instead, it is a general concensus that the copper-bis(dithiolene) coordination motif, as a whole, functions as an electron reservoir to facilitate complex redox switchings. The above-discussed spectroscopic characterizations for GCPs **1** and **2** are unable to distinguish whether a Cu ion is Cu(I) or Cu(II) in the structures. In this case, they can be classified as Class III mixed-valence structures,[17] i.e. Creutz-Taube structures, according to the Robin-Day classification.[18] More importantly, we addressed a long-standing controversy about the oxidation states of metal ions in such 2D materials, and demonstrated that a periodic atomic structure could host a different number of electrons but remain charge neutral.

With a different number of total electrons, GCPs **1** and **2** should give rise to distinct electron configurations that would be reflected in some macroscale features, such as optical properties and electrical conductivity. As shown in Figure S12, GCP **1** shows a much lower reflection than GCP **2** across the 400 – 1100 nm range. This could be a direct experimental evidence for their distinct electronic structures, since this wavelength range is not possible for phonon vibrations. Besides, a near-constant electrical conductivity profile was recorded for the pressed pellet of GCP **1** using four-point method,[19] stabilizing at about 187 S/cm across the 3 – 300 K range (Figure S13a). In the literature, the electrical conductivity of GCP **2** was reported as 280 S/cm,[5a] and our synthesized GCP **2** shows a lower but comparable result of *ca.* 130 S/cm (Figure S13b). It is worth noting that the conductivity of GCP **2** also remained nearly constant across the 3 – 300 K range, suggesting that the temperature-independent electrical conductivity could be a common character of 2D Cu-BHT GCPs, regardless of the Cu oxidation states. In comparison, the 3D Cu(I)-BHT $[Cu_4C_6S_6]_n$ and $[Cu_{5.5}C_6S_6]_n$ both display typical conductivity profiles of semiconductors, with a significant decrease upon cooling.[9]

Theoretical calculations are essential for such novel materials to decode their detailed structures and formation mechanism. However, it is a grand challenge to model these two GCPs, because they are neutral isostructures yet possessing a different number of total electrons, making them a unique pair of isostructures with hetero-electronic configurations. We herein employ both periodic and cluster models to simulate these GCPs (Figure S14a and b). The neutral double-layer periodic model was constructed as GCP **1**, and hence GCP **2** was mimicked by removing three electrons from the model (with six Cu ions per unit) to simulate the scenario where half of the Cu ions in the model were oxidized from Cu(I) to Cu(II). The same concept is also used for the cluster model building, with the neutral cluster as GCP **1** and that with six electrons less as GCP **2**. These models may not precisely represent the actual situation, but we expect to gain insight into their electronic responses by changing the total number of electrons in the systems.

We carried out the high accuracy DFT calculations with hybrid exchange-correlation functionals (HSE06) for the periodic model to reveal the intrinsic coordination valence in GCPs **1** and **2**. As shown in **Table 1**, the lattice parameters and interlayer distances of GCP **1** and **2** are almost identical with less than 3% variations, which agree with their near identical XRD patterns. However, the total number of electrons hosted in GCP **1** and **2** are different, so the Bader charges on each type of element vary. Interestingly, after removing three electrons, the charges on Cu only change slightly from +0.597 in GCP **1** to +0.708 in GCP **2**. However, this is in contrast to the -0.203 charge on the S atoms in GCP **1**, of which those in GCP **2** seem to

be completely absent, indicating the role of S atoms located at the five-membered coordination rings as an electron reservoir. In other words, the effect of adding electrons to or removing electrons from the structure is mainly reflected on BHT ligands. We further demonstrate such charge density redistribution in Figure S15, where the charge density differences between these two GCPs are found primarily on the BHT ligands. Similar results were also obtained using the cluster model (Table S1).

Table 1. The total charge per $[Cu_3C_6S_6]_2$ unit cell Q_0 (in elementary charge e_0), lattice parameters and interlayer distance d at HSE06+vdW level, the Bader charges q^B, the spin moments $\boldsymbol{m}$ on atomic sites in one layer of Cu-BHT. The superscripts for the spin moments $\boldsymbol{m}$ indicate the degeneracy of the atomic site. The spin moments of atoms on the adjacent layer take opposite signs; therefore, the whole system possesses an interlayer-AFM ground state. Here, $Q_0 = 0e_0$ state represents GCP **1** and $Q_0 = +3e_0$ state is for GCP **2**. For further illustration of the electron reservoir effect of BHT, the state *of* $Q_0 = -3e_0$ is also shown, representing a situation wherein electrons were added to the system. All structures are in A2/m symmetry, and the lattice parameters are reported for primitive cells.

$\boldsymbol{Q_0(e_0)}$	***+3*** (GCP **2**)	***0*** (GCP **1**)	***-3***
a = b (Å)	8.69	8.71	8.70
c (Å)	7.64	7.91	7.48
α = β (°)	64.67	63.61	68.75
γ (°)	59.89	59.74	59.34
d (Å)	3.32	3.40	3.37
$\boldsymbol{q^B_{Cu}}$	0.708±0.005	0.597±0.010	0.478±0.041
$\boldsymbol{q^B_C}$	-0.102±0.049	-0.096±0.038	-0.166±0.023
$\boldsymbol{q^B_S}$	-0.003±0.016	-0.203±0.025	-0.323±0.003
$\boldsymbol{m^1_{Cu}}$	0.350	0.294	0.278
$\boldsymbol{m^2_{Cu}}$	0.360	0.213	-0.013
$\boldsymbol{m^1_C}$	-0.050	0.021	0.002
$\boldsymbol{m^2_C}$	-0.006	0.005	0.003
$\boldsymbol{m^1_S}$	0.077	0.117	-0.010
$\boldsymbol{m^2_S}$	-0.013	-0.012	0.062

These calculation results agree well with our proposed mechanism that the three radicals on each BHT can either oxidize three out of six coordinated Cu(I) to Cu(II) in the formation of GCP **1**, or reduce three Cu(II) to Cu(I) in GCP **2**. The radicals are either fully paired in the

oxidation reaction or completely annihilated from BHT ligands in the reduction reaction (Figure 1a). We call the above mechanism an intramolecular *pseudo*-redox process. Since such redox reactions occur between the metals and ligands, it affects little on the atomic structures, which would be the reason behind the formation of these two isostructures with hetero-electronic configurations. Our HSE06 calculations further confirm that majority of the magnetic moments are located on Cu ions (Table 1), which couple FM within a single layer. At the same time, the calculated ground state is interlayer AFM, in accordance with our magnetic susceptibility measurements. The calculated energy of the in-plane FM state is 13 meV lower than that of the ferrimagnetic state generated by flipping one local spin moment on Cu sites. This implies an unavoidable spin fluctuation and extremely low Curie Temperature, which agrees with the fact that no long-range magnetic ordering was detected above the lowest temperature attained in our experiment (i.e. 4 K). In addition, our calculations identify two types of Cu ions in a single layer of the periodic model (Figure S14a). They carry slightly different Bader charges and spin moments, correlated via BHT intermediation and FM coupled with each other in a double-exchange mechanism.

Unlike the commonly reported linear mixed-valence structures,[20] Cu ions in these 2D GCPs form a hexagon around the BHT bridging sites. As a result, electron hopping can easily occur between any two adjacent Cu ions, promoting the high charge delocalization and electrical conductivity in the 2D sheets. Our calculated band structures confirm their highly conductive features, where the bands cross the Fermi level dispersively. In addition, based on the projected densities of states (pDOSs, Figure S16) and the projected fat bands in band structures based on Mulliken analysis (Figure S17), the bands around the Fermi level seem to be dominantly contributed by S atoms, with only trace presence of the Cu d-orbitals within ±1.0 eV. The positions of the d-orbital bands only show minor changes when the total system charge varies, consistent with the above-mentioned Bader charge analysis. Both systems are metallic and should possess high electrical conductivity, which agrees with our experimental measurements.

The BHT ligand seems unique from those in traditional Creutz-Taube mixed-valence complexes, wherein the ligands normally can be easily reduced but not oxidized. We ascribe this uniqueness to the radicals on BHT, of which the energy level is located between Cu(I) and Cu(II), so that it can either be reduced when coordinated with Cu(I), or be oxidized when coordinated with Cu(II) (see Figure S18 for a conceptual illustration). This provides a general guideline for selecting suitable ligands to prepare other 2D Creutz-Taube structures.

3. Conclusion

In summary, we report the first example of Cu(I)-BHT graphene-like 2D conjugated coordination polymers (GCPs) via elaborately designed chemical reactions. Furthermore, we demonstrated using the same ligands (BHT) coordinated with Cu(I) and Cu(II) ions, one can construct a pair of 2D isostructures. Leveraging on DFT calculations, we further uncovered an intramolecular *pseudo*-redox mechanism, where the BHT ligands act as either oxidants or reductants to oxidize Cu(I) or reduce Cu(II), eventually forming mixed-valence isostructural GCPs. The spectroscopically indistinguishable Cu(I) and Cu(II) ions coexist in both GCPs, exhibiting an average fractional oxidation state of +1.5, making these two GCPs typical Creutz–Taube structures. For the first time, we elucidate how a charge-neutral periodic atomic structure can host a different number of electrons, which could be a new milestone in chemistry, physics, and material science. We believe this work will stimulate further fundamental and translational research efforts in such exciting mixed-valence 2D materials in time to come.

4. Experimental Section/Methods

*Synthesis of GCP **1** and **2***: All chemicals were purchased from commercial sources and used as received unless otherwise stated. The synthetic operations were all conducted with a standard Schlenk line protected with N_2. For synthesis of GCP **1**, to a 100 mL Schlenk tube ethanol (15 mL), DI water (30 mL) and KI (10 g) were added and stirred to form a clear solution. The Schlenk tube was sealed with a rubber septum and bubbled with N_2 using a cannula for 10 min to remove residual O_2 in the solution. Copper iodide (CuI, 422.5 mg, 2.22 mmol) was then added and stirred at room temperature for 1 hour to form a clear pale-yellow solution. Benzenehexathiol (BHT, 200 mg, 0.74 mmol) was added as solid powder with a stainless steel spatula. The pale-yellow suspension was further stirred at room temperature for 2 days, which was gradually turned to a black suspension. The black powdery crude product was isolated by centrifuge, washed with water (2×10 mL) and ethanol (2×10 mL) successively. The product was dried overnight in vacuum, affording 329 mg product as a fine black powder (isolated yield 98%). For synthesis of GCP **2**, we followed a literature procedure.[5a] In brief, to a 100 mL Schlenk tube, ethanol (30 mL) and $CuCl_2$ (300 mg, 2.23 mmol) were mixed and stirred to form a green solution. BHT powder (200 mg, 0.74 mmol) was then added to form a yellow slurry, which was stirred for 2 days to afford a black suspension. The product was isolated by centrifuge, washed with water (2×10 mL) and ethanol (2×10 mL) successively, and dried overnight in vacuum, affording 325 mg product as a fine black powder (isolated yield 96%).

Materials Characterization: FESEM images and energy-dispersive X-ray (EDX) spectra were recorded using a JOEL JSM 7600F with an Oxford ISIS X-ray EDX microanalysis system, with 5 and 15 kV applied voltages for imaging and EDX studies, respectively. Au or Pt sputtering was applied on the sample to improve electrical conductivity. TEM images were obtained on a JEOL JEM-2100F field emission transmission electron microscope with 200 kV acceleration voltage. Powder XRD was performed using Bruker D8 Discover GADDS 1.5418 Å (40 kV, 40 mA). The XPS data was obtained using Thermal Scientific Theta Probe equipment with a monochromatized Al Kα X-ray source of 1486.71 eV photons, a pass energy of 200 eV for survey scan and 40 eV for high resolution scan, and a photoelectron take-off angle (α) of 50° with respect to surface normal. Elemental analysis was conducted using THERMO SCIENTIFIC Elemental Analyzer (FLASH EA 1112). UV-Vis diffuse reflectance was recorded using a Shimadzu UV3600 UV-Vis-NIR spectrophotometer, with $BaSO_4$ as the reference. The ESR data was collected using JEOL FA200 ESR spectrometer. For magnetic susceptibility measurement, the powder sample was encapsulated with Al foil, then characterized for their magnetic properties using a superconducting quantum interference device (SQUID) magnetometer. The sample was cooled to 4 K under a zero magnetic field, Then, they were heated to 300K under a magnetic field of 1 kOe, during which a magnetization (M) *vs.* temperature (T) heating measurement was obtained. Subsequently, they were cooled without field during which another M-T cooling measurement was obtained. X-ray magnetic circular dichroism spectroscopy (XMCD) was performed by X-ray absorption spectroscopy of Cu-$L_{2,3}$ edge under room temperature at beamline SINS (Surface, Interface and Nanostructure Science) of SSLS (Singapore Synchrotron Light Source), with the X-ray beam size of 0.2×0.2 mm^2. The XANES and EXAFS measurements were carried out at the XAFCA beamline of SSLS. The EXAFS data were analyzed using the Demeter software package. All characterization results of GCP **2** are given in the Extended Data together with that of GCP **1** for easy comparison.

Computational Methods for the Periodic Model: We carried out structural optimization with all-electron FHI-aims package[21] for periodic mode, using HSE06 hybrid functional[22] to account the possible electron correlation and the effect of radicals. Long-range van der Waals interactions were taken into consideration via the Tkatchenko and Scheffler (TS) scheme[23] to describe the interlayer interaction accurately. Double-layered models were employed to accommodate the possible interlayer antiferromagnetic (AFM) state. Monkhorst-Pack method was employed to generate the k-mesh and the k-point sampling was set to 2×2×2 for structural optimization and 5×5×5 for band structure and property calculations, respectively. The lattice constants and atomic positions are fully relaxed structural optimization. The maximum residual

force component on each atom was optimized until smaller than 5×10^{-3} eV $Å^{-1}$. Thereafter, the lattice parameters of *pseudo*-AB and AA stacking structures are refined against the experimentally measured XRD using Rietveld[24] method by fixing atomic fractional coordinates. Besides, the scalar-relativistic effect was treated at the level of atomic ZORA approximation,[21] and the effects of spin-orbital coupling were also included in post-processed features of FHI-aims.[25] The Bader charges[26] were calculated using analysis program developed by Henkelman group.[27] Meanwhile, the atomic local magnetizations were calculated using the Bader charge analysis program by feeding in the spin density while keeping the spatial division for charge density. The charge densities are visualized using Visualization for Electronic and Structural Analysis (VESTA).[28]

Computational Methods for the Cluster Model: We use Gaussian 16 package[29] with UB3LYP hybrid functional[30] for cluster models structural optimization. The ground-state and the first excited state were optimized using 6-31G basis-set, followed by time-dependent density-functional theory (TD-DFT) calculations with 6-31G(d,p) basis-set.

Supporting Information

Supporting Information is available from the author.

Acknowledgements

We gratefully acknowledge the support from IMRE-A*STAR (project code: SC25/21-102319), AME YIRG (Grant No.: A2084c0174), and SERC-A*STAR (Grant Nos.: 1527200020, 1527200024, A1898b0043). Special thanks go to Ms. Doreen Mei Ying Lai (IMRE) for FESEM, Ms. Siew Lang Teo (IMRE) for TEM, and Ms. Seah Kim Kui Georgina Estelle (IMRE) for elemental analysis.

Received: ((will be filled in by the editorial staff))
Revised: ((will be filled in by the editorial staff))
Published online: ((will be filled in by the editorial staff))

References

[1] M. Hmadeh, Z. Lu, Z. Liu, F. Gándara, H. Furukawa, S. Wan, V. Augustyn, R. Chang, L. Liao, F. Zhou, E. Perre, V. Ozolins, K. Suenaga, X. Duan, B. Dunn, Y. Yamamto, O. Terasaki, O. M. Yaghi, *Chem. Mater.* **2012**, 24, 3511.

[2] a) H. Banda, J.-H. Dou, T. Chen, N. J. Libretto, M. Chaudhary, G. M. Bernard, J. T. Miller, V. K. Michaelis, M. Dincă, *J. Am. Chem. Soc.* **2021**, 143, 2285; b) J. Park, M. Lee, D. Feng, Z. Huang, A. C. Hinckley, A. Yakovenko, X. Zou, Y. Cui, Z. Bao, *J. Am. Chem. Soc.* **2018**, 140, 10315; c) K. Wada, K. Sakaushi, S. Sasaki, H. Nishihara, *Angew. Chem. Int. Ed.* **2018**, 57, 8886; d) M. Ko, L. Mendecki, K. A. Mirica, *Chem. Commun.* **2018**, 54, 7873.

[3] L. S. Xie, G. Skorupskii, M. Dincă, *Chem. Rev.* **2020**, 120, 8536.

[4] a) T. Kambe, R. Sakamoto, K. Hoshiko, K. Takada, M. Miyachi, J.-H. Ryu, S. Sasaki, J. Kim, K. Nakazato, M. Takata, H. Nishihara, *J. Am. Chem. Soc.* **2013**, 135, 2462; b) T. Kambe, R. Sakamoto, T. Kusamoto, T. Pal, N. Fukui, K. Hoshiko, T. Shimojima, Z. Wang, T. Hirahara, K. Ishizaka, S. Hasegawa, F. Liu, H. Nishihara, *J. Am. Chem. Soc.* **2014**, 136, 14357; c) A. J. Clough, J. W. Yoo, M. H. Mecklenburg, S. C. Marinescu, *J. Am. Chem. Soc.* **2015**, 137, 118; d) X. Huang, P. Sheng, Z. Tu, F. Zhang, J. Wang, H. Geng, Y. Zou, C.-a. Di, Y. Yi, Y. Sun, W. Xu, D. Zhu, *Nat. Commun.* **2015**, 6, 7408; e) T. Pal, S. Doi, H. Maeda, K. Wada, C. M. Tan, N. Fukui, R. Sakamoto, S. Tsuneyuki, S. Sasaki, H. Nishihara, *Chem. Sci.* **2019**, 10, 5218; f) N. Lahiri, N. Lotfizadeh, R. Tsuchikawa, V. V. Deshpande, J. Louie, *J. Am. Chem. Soc.* **2017**, 139, 19.

[5] a) X. Huang, H. Yao, Y. Cui, W. Hao, J. Zhu, W. Xu, D. Zhu, *ACS Appl. Mater. Interfaces* **2017**, 9, 40752; b) X. Huang, S. Zhang, L. Liu, L. Yu, G. Chen, W. Xu, D. Zhu, *Angew. Chem. Int. Ed.* **2018**, 57, 146.

[6] a) K. Fan, C. Zhang, Y. Chen, Y. Wu, C. Wang, *Chem* **2021**, 7, 1224; b) R. Kato, *Chem. Rev.* **2004**, 104, 5319.

[7] T. Takenaka, K. Ishihara, M. Roppongi, Y. Miao, Y. Mizukami, T. Makita, J. Tsurumi, S. Watanabe, J. Takeya, M. Yamashita, K. Torizuka, Y. Uwatoko, T. Sasaki, X. Huang, W. Xu, D. Zhu, N. Su, J. G. Cheng, T. Shibauchi, K. Hashimoto, *Sci. Adv.*, 7, eabf3996.

[8] a) P. M. Cheung, R. F. Berger, L. N. Zakharov, J. D. Gilbertson, *Chem. Commun.* **2016**, 52, 4156; b) E. W. Dahl, N. K. Szymczak, *Angew. Chem. Int. Ed.* **2016**, 55, 3101.

[9] X. Huang, Y. Qiu, Y. Wang, L. Liu, X. Wu, Y. Liang, Y. Cui, Y. Sun, Y. Zou, J. Zhu, W. Fang, J. Sun, W. Xu, D. Zhu, *Angew. Chem. Int. Ed.* **2020**, 59, 22602.

[10] a) C. Creutz, H. Taube, *J. Am. Chem. Soc.* **1969**, 91, 3988; b) C. Creutz, H. Taube, *J. Am. Chem. Soc.* **1973**, 95, 1086.

[11] J. Park, A. C. Hinckley, Z. Huang, D. Feng, A. A. Yakovenko, M. Lee, S. Chen, X. Zou, Z. Bao, *J. Am. Chem. Soc.* **2018**, 140, 14533.

[12] X. Zhou, J. Dong, Y. Zhu, L. Liu, Y. Jiao, H. Li, Y. Han, K. Davey, Q. Xu, Y. Zheng, S.-Z. Qiao, *J. Am. Chem. Soc.* **2021**, 143, 6681.

[13] W.-J. Sun, H.-Q. Ji, L.-X. Li, H.-Y. Zhang, Z.-K. Wang, J.-H. He, J.-M. Lu, *Angew. Chem. Int. Ed.* **2021**, 60, 22933.

[14] T. Geetha Kumary, J. G. Lin, *J. Appl. Phys.* **2008**, 103, 053913.

[15] T. Berry, J. R. Morey, K. E. Arpino, J.-H. Dou, C. Felser, M. Dincă, T. M. McQueen, *Inorg. Chem.* **2022**, 61, 6480.

[16] I. Felner, *Magnetochemistry* **2016**, 2, 34.

[17] a) R. M. Stolz, A. Mahdavi-Shakib, B. G. Frederick, K. A. Mirica, *Chem. Mater.* **2020**, 32, 7639; b) L. B. Zasada, L. Guio, A. A. Kamin, D. Dhakal, M. Monahan, G. T. Seidler, C. K. Luscombe, D. J. Xiao, *J. Am. Chem. Soc.* **2022**, 144, 4515.

[18] M. B. Robin, P. Day, in *Advances in Inorganic Chemistry and Radiochemistry*, Vol. 10 (Eds: H. J. Emeléus, A. G. Sharpe), Academic Press, 1968.

[19] Q. Li, V. Thangadurai, *J. Mater. Chem.* **2010**, 20, 7970.

[20] W. Grochala, R. Hoffmann, *Angew. Chem. Int. Ed.* **2001**, 40, 2742.

[21] V. Blum, R. Gehrke, F. Hanke, P. Havu, V. Havu, X. Ren, K. Reuter, M. Scheffler, *Comput. Phys. Commun.* **2009**, 180, 2175.

[22] J. Paier, M. Marsman, K. Hummer, G. Kresse, I. C. Gerber, J. G. Ángyán, *J. Chem. Phys.* **2006**, 124, 154709.

[23] A. Tkatchenko, M. Scheffler, *Phys. Rev. Lett.* **2009**, 102, 073005.

[24] R. A. Young, *Oxford University Press* **1993**, 5.

[25] W. P. Huhn, V. Blum, *Phys. Rev. Mater.* **2017**, 1, 033803.

[26] R. F. W. Bader, *Acc. Chem. Res.* **1985**, 18, 9.

[27] a) Tang. E, Sanville. E, Henkelman. G, *J. Phys.: Condens. Matter* **2009**, 21, 084204; b) M. Yu, D. R. Trinkle, *J. Chem. Phys.* **2011**, 134, 064111.

[28] K. Momma, F. Izumi, *J. Appl. Cryst.* **2008**, 41, 653.

[29] M. J. Frisch, G. W. T., et al., , Gaussian 16, Revision C.01, Gaussian, Inc., Wallingford CT. **2016**.

[30] A. D. Becke, *J. Chem. Phys.* **1993**, 98, 1372.

We report a pair of isostructural Cu(I)/Cu(II) mixed-valence Creutz-Taube 2D coordination polymers prepared using Cu(I) and Cu(II) precursors, and uncovered an intramolecular *pseudo*-redox mechanism during their formation. This work addressed a long-standing controversy about metal ion oxidation states in 2D structures, and more importantly unveiled an unusual fact that neutral 2D coordination polymers can host a different number of total electrons as ground states without significant structural changes.

Ning Li,‡ Gang Wu,‡ Shibo Xi,‡ Fengxia Wei, Ming Lin, Jinjun Qiu, Jin-Cheng Zheng, Jiabao Yi, Debbie Hwee Leng Seng, Coryl Jing Jun Lee, D. V. Maheswar Repaka, Xiaoming Liu, Zicong Marvin Wong, Qiang Zhu, Shuo-Wang Yang* and He-Kuan Luo*

Cu(I)/Cu(II) Creutz-Taube Mixed-Valence 2D Coordination Polymers

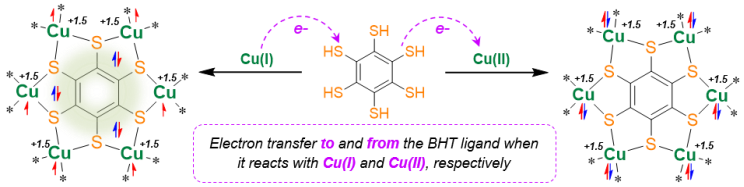

Supporting Information

Cu(I)/Cu(II) Creutz-Taube Mixed-Valence 2D Coordination Polymers

Ning Li,‡ Gang Wu,‡ Shibo Xi,‡ Fengxia Wei, Ming Lin, Jinjun Qiu, Jin-Cheng Zheng, Jiabao Yi, Debbie Hwee Leng Seng, Coryl Jing Jun Lee, D. V. Maheswar Repaka, Xiaoming Liu, Zicong Marvin Wong, Qiang Zhu, Shuo-Wang Yang and He-Kuan Luo**

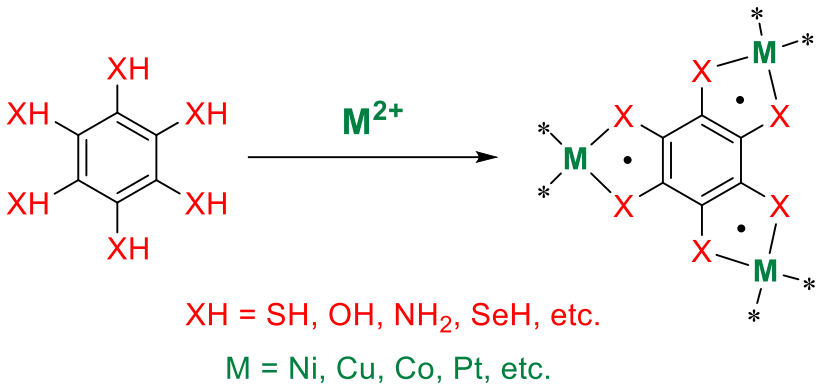

Figure S1. Typical synthesis and structures of 2D coordination polymers with porous Kagomé lattices. Radicals in the five-membered coordination rings are also indicated.

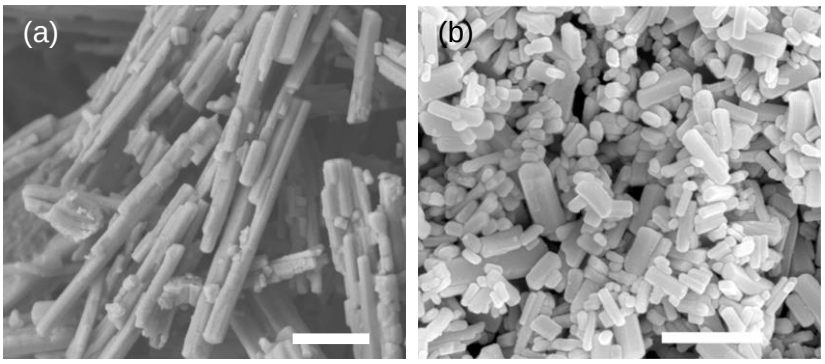

Figure S2. FESEM images of GCP **2**: (a) sample prepared in our lab, and (b) the image reported in *ACS Appl. Mater. Interfaces*, **2017**, *9*, 40752 – 40759. Scale bars in panel (a) and (b) are 1 μm and 2 μm, respectively. We attribute the morphology difference in aspect ratio of the nanorods to the different sources of BHT ligands used.

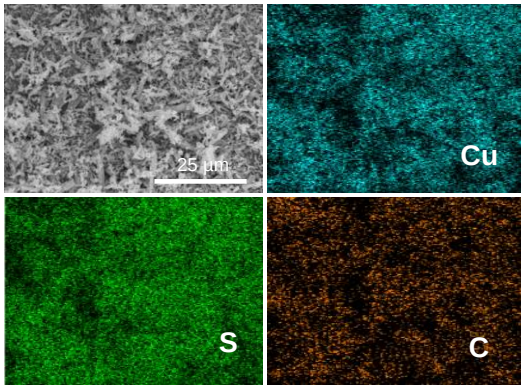

Figure S3. FESEM-EDX elemental mapping for Cu, S and C in GCP **1**, confirming homogeneous elemental distribution across the polycrystalline powder sample.

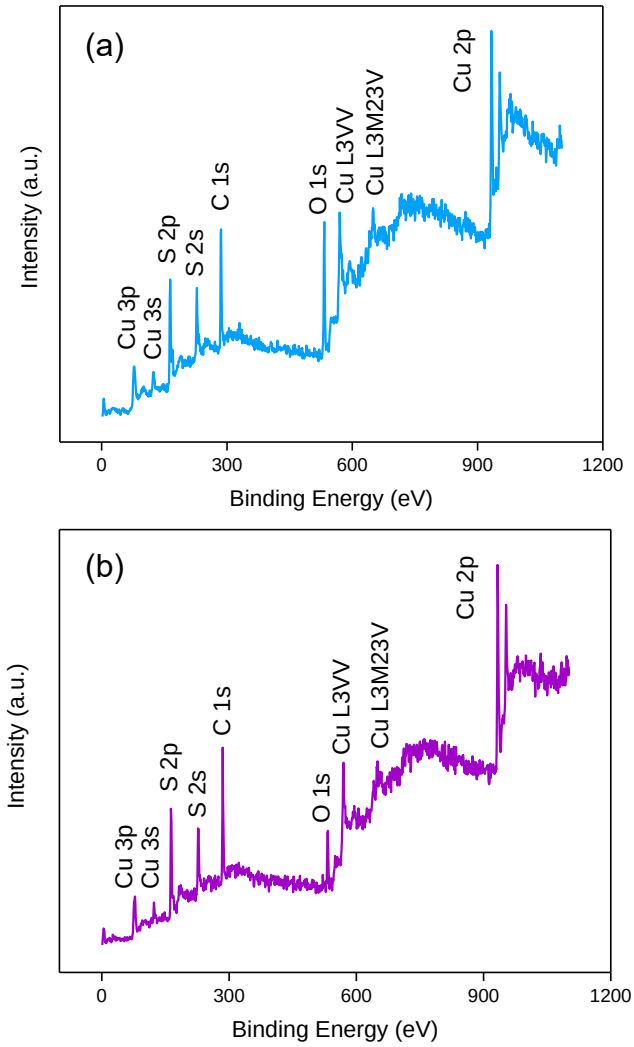

Figure S4. XPS survey scan for (a) GCP **1** and (b) GCP **2,** showing the presence of C, S, Cu. The *1s* signal of O was also detected, possibly due to the O_2/H_2O impurities adsorbed on the surface. No signals of K or I was seen, confirming the absence of counter ions.

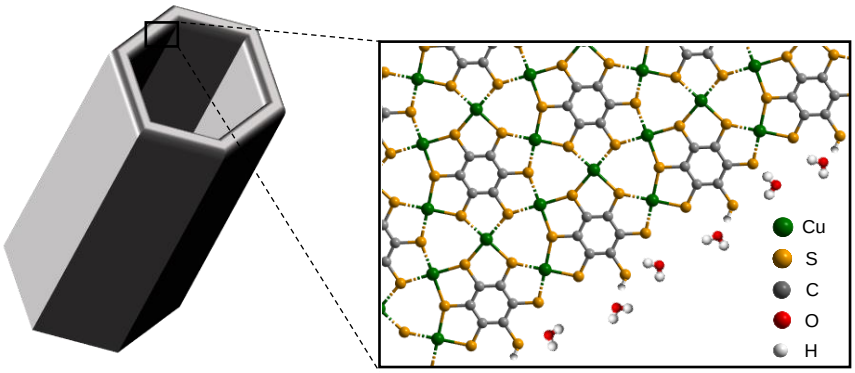

Figure S5. Schematic illustration of possible surface coordination structure of GCP **1** microcrystalline blocks. Some thiol groups may be dangling with possible water adsorption via hydrogen bonding, giving rise to a slightly lower Cu:S ratio in the overall structure (0.48:1, determined by FESEM-EDX) and detectable O signals in XPS analysis.

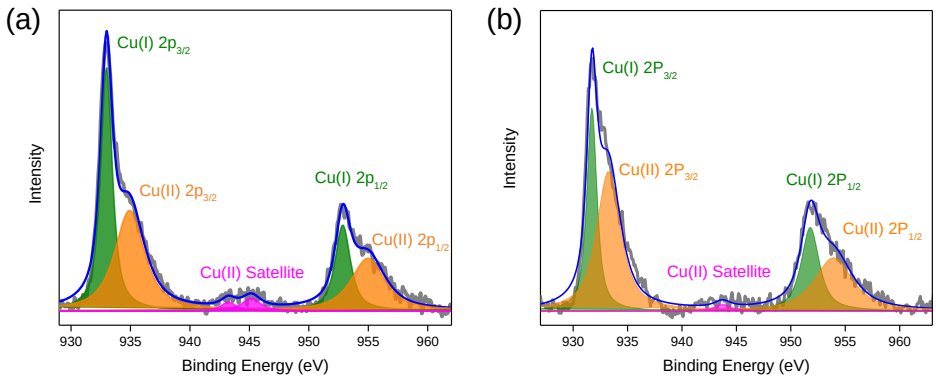

Figure S6. Comparison of the high-resolution XPS Cu *2p* scan of GCP (a) **1** and (b) **2**. Panel (a) is identical to Figure 3b in the main text.

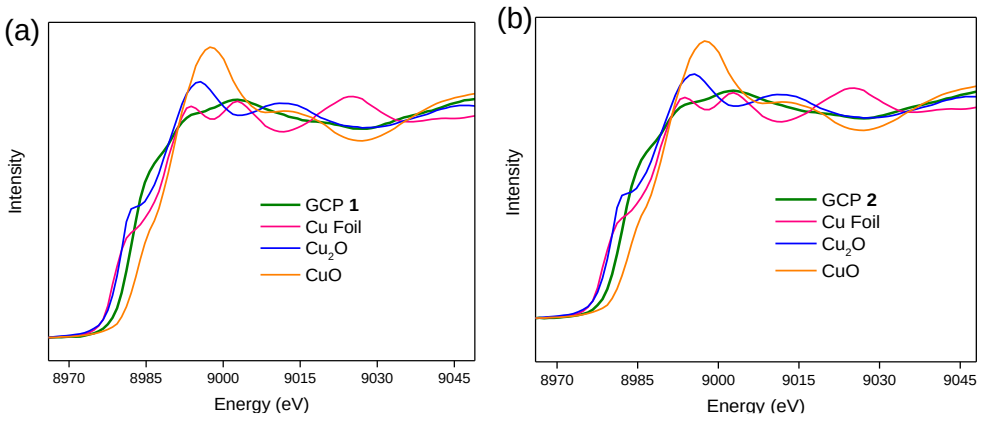

Figure S7. Comparison of the Cu K-edge XANES spectra of GCP (a) **1** and (b) **2**. Panel (a) is identical to Figure 3c in the main text.

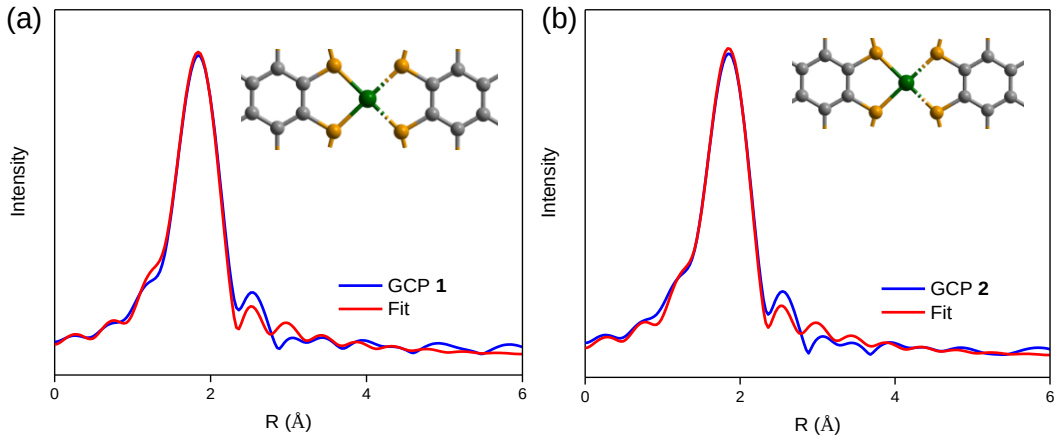

Figure S8. Comparison of the experimental and simulated EXAFS spectra of GCP (a) **1** and (b) **2**. Data fitting suggests an average Cu coordination number of 4.2(5) and Cu-S bond length of 2.287(9) Å in GCP **1**, and 4.0(5) and 2.292(8) Å for GCP **2**. We note that the actual bond length is usually 0.2 – 0.5 Å longer than the EXAFS peak position due to scattering phase shift.

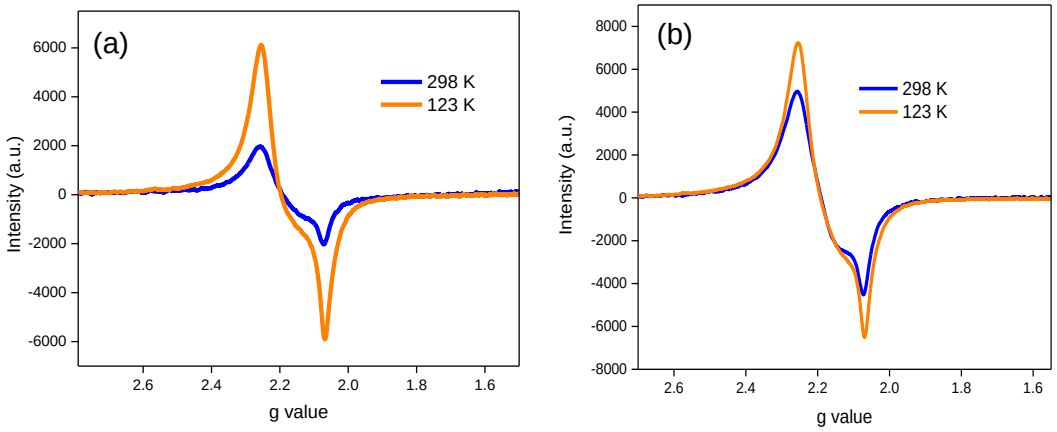

Figure S9. Comparison of the ESR spectra of GCP (a) **1** and (b) **2.** Panel (a) is identical to Figure 3d in the main text.

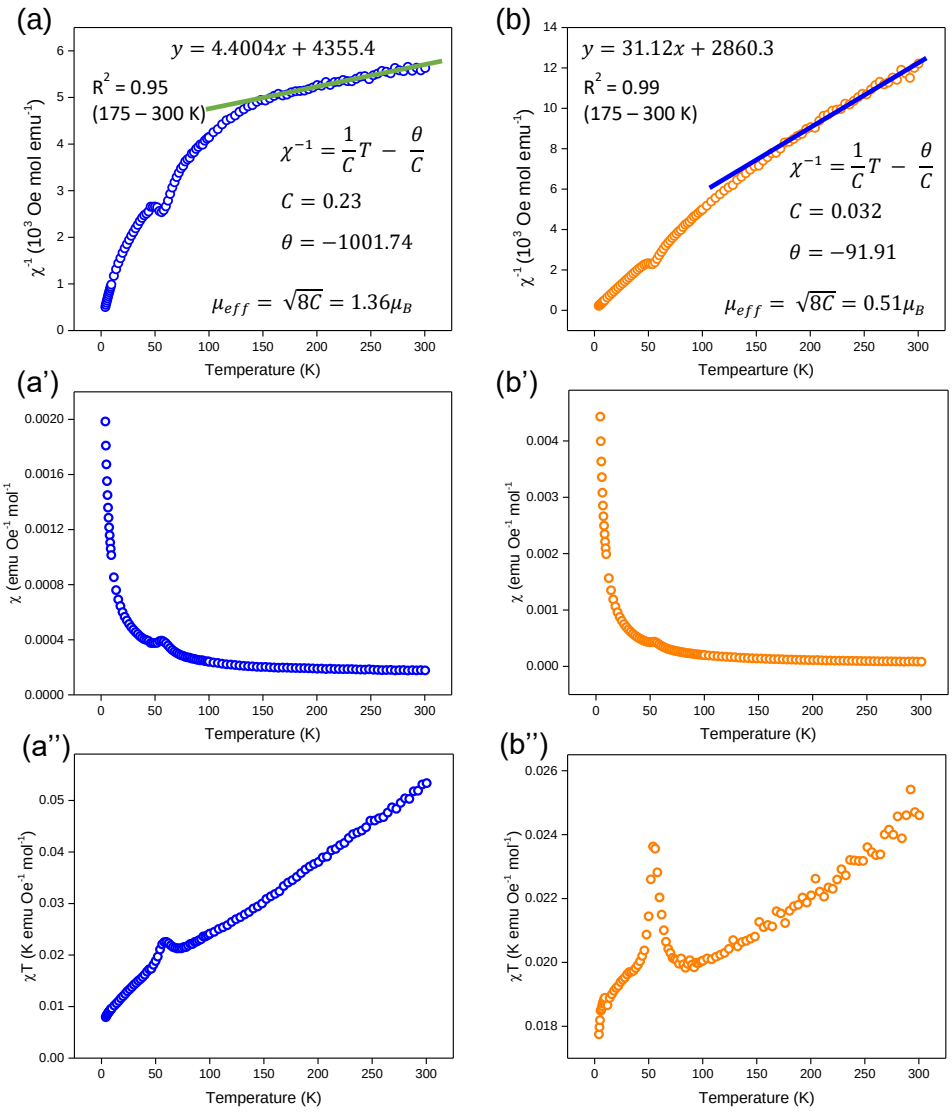

Figure S10. Comparison of the magnetic behaviors of GCP (a) **1** and (b) **2**. The profile in panel (a) is identical to Figure 3e in the main text. Calculations for effective magnetic moment for each Cu center based on Curie-Weiss Law are also shown. The shoulder at around 52 K was ascribed to the liquid oxygen.

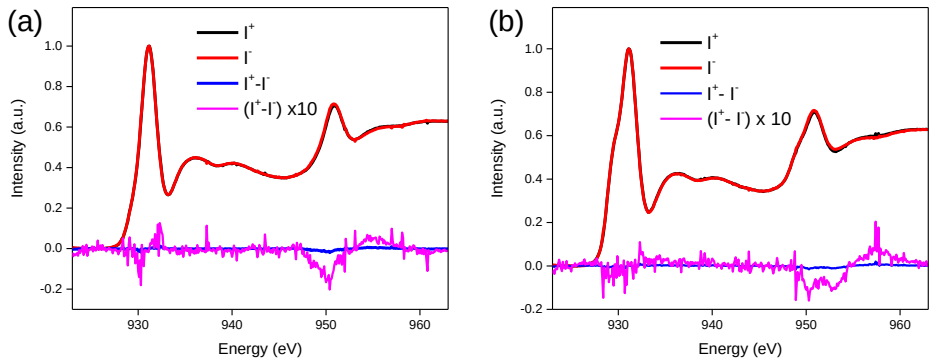

Figure S11. Comparison of the XMCD spectra of GCP (a) **1** and (b) **2**. Panel (a) is identical to Figure 3f in the main text.

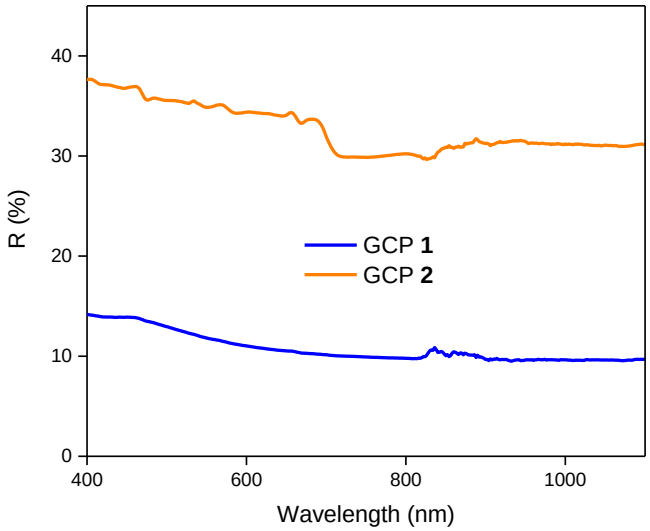

Figure S12. Experimental UV-Vis-NIR reflection profile of GCP **1** and **2**.

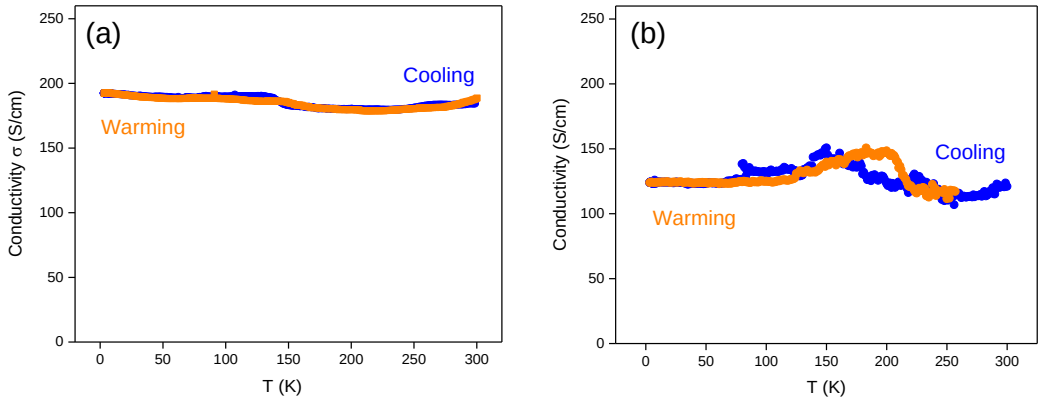

Figure S13. Comparison of the temperature-dependent electrical conductivity profile of GCP (a) **1** and (b) **2** using pressed pellet sample and four-point measurement method. For the almost temperature-independent conductivity, it can be explained as follows. The inter-grain hopping of polycrystalline pressed pellet samples usually plays a dominant role in determining the bulk electrical conductivity. Such hopping renders the bulk material with apparent semiconducting features, showing decreased conductivity upon cooling. On the contrary, each of the nanocrystallites is metallic in nature, confirmed by our calculations and previous reports (*Nat. Commun.*, **2015**, *6*, 7408). Metallic materials display increasing electrical conductivity upon cooling, as the carrier scattering due to lattice vibrations dominates the charge transport. These opposing mechanisms (metallic vs. semiconducting) appear to be both present in the pressed pellet of GCP **1** and **2**, and their influences likely cancel each other out, leading to the near-constant conductivity profile.

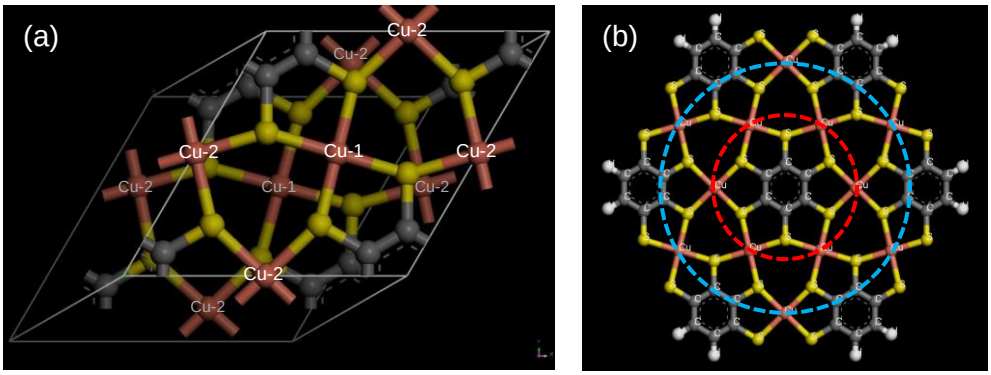

Figure S14. (a) The periodic GCP model, where two distinct Cu sites are labelled as Cu-1 and Cu-2 according to their symmetric degeneracies. (b) The cluster model with two shells of Cu atoms highlighted by the red and blue circles, respectively.

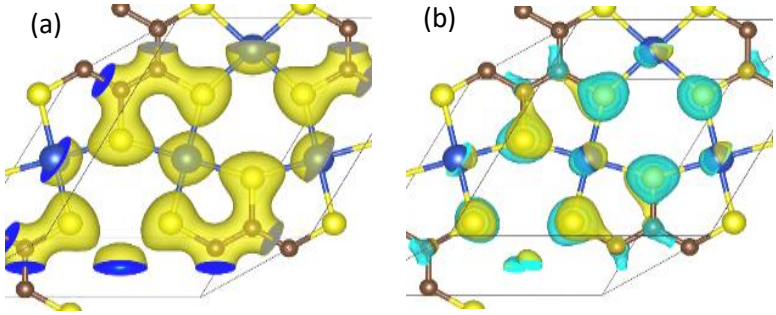

Figure S15. (a) Neutral Cu-BHT ($Q_0 = 0e_0$) with isovalue of 0.08 Å^{-3}, representing GCP **1**. (b) The charge density difference between GCP **2** ($Q_0 = +3e_0$) and GCP **1** ($Q_0 = 0e_0$) with isovalue of 0.02 Å^{-3}.

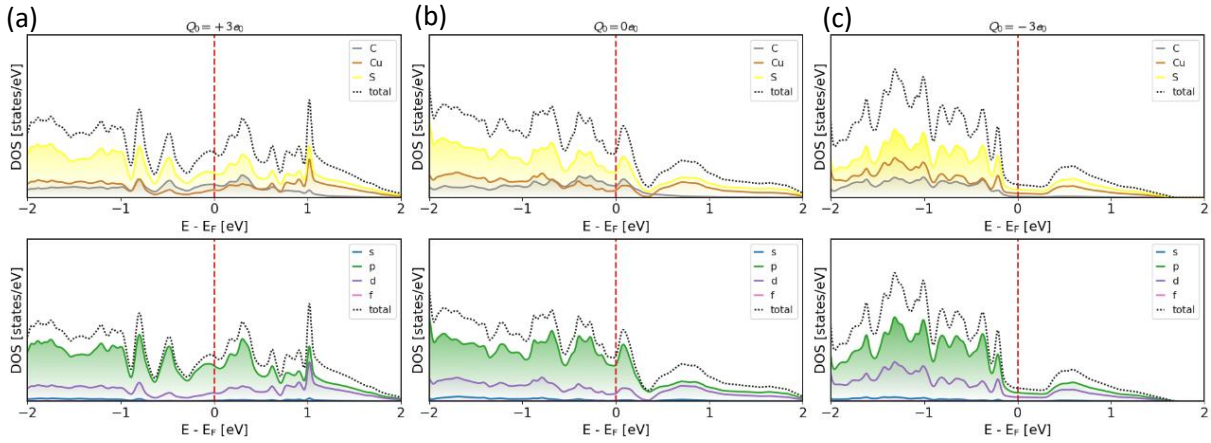

Figure S16. The projected densities of states (pDOSs) for (a) $+3e_0$ (GCP **2**), (b) Neutral (GCP **1**), and (c) $-3e_0$ systems. Note that pDOSs are based on Mulliken analysis with arbitrarily chosen overlapping basis set, so the projections on species are just presented for qualitative analyses.

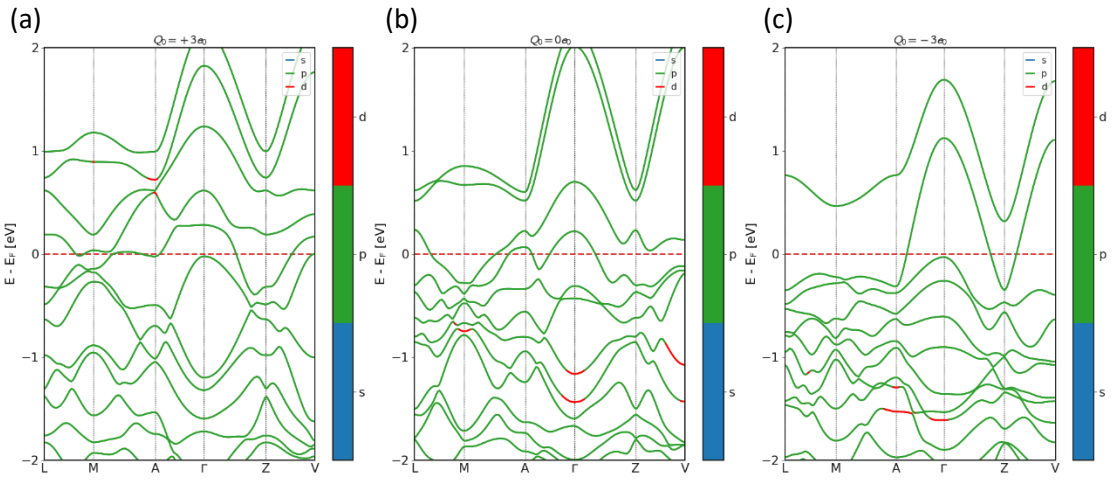

Figure S17. The projected fat bands for (a) +3e_0 (GCP **2**), (b) Neutral (GCP **1**), and (c) -3e_0 systems. The calculated band structures indicate both GCPs **1** and **2** are very good electrical conductors, agreeing with our experimental measurements.

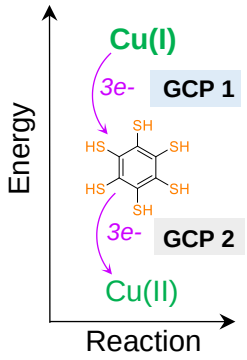

Figure S18. Simplified energy diagram of BHT ligand, Cu(I), and Cu(II) ions.

Table S1. The total charge per [$Cu_{12}C_{42}S_{30}H_{12}$] cluster Q_0 (in elementary charge e_0), and the dipole-moment-corrected Hirshfeld charges q, Mulliken spin moments m on atomic sites. The superscripts 'in' or 'out' means that the corresponding atom is located on the inner or outer circles shown in Figure S14b. The spin moments of Cu on the inner circle are arranged in AFM configuration, and here only the absolute values are given. $Q_0 = 0e_0$ represents GCP **1** and $Q_0 = +6e_0$ represents GCP **2**. For further illustration of the electron reservoir effect of BHT, the state of $Q0 = -6e_0$ is also shown, representing a situation wherein electrons were added to the system.

Q_0 (E_0)	+6	0	-6
q_{Cu}^{in}	0.608±0.114	0.601±0.040	0.585±0.014
q_{Cu}^{out}	0.480±0.095	0.460±0.078	0.552±0.061
q_{S}^{in}	-0.250±0.075	-0.362±0.219	-0.345±0.012
q_{C}^{out}	0.016±0.121	0.037±0.194	0.015±0.006
m_{Cu}^{in}	0.483±0.018	0.479±0.024	0.496±0.020